JOURNAL OF SOLID STATE CHEMISTRY 103, 1–15 (1993)

The Crystal Chemistry and Physical Properties of the Triple Layer Perovskite Intergrowths $LaSr_3Fe_3O_{10-\delta}$ and $LaSr_3(Fe_{3-x}Al_x)O_{10-\delta}$

J. Y. LEE, J. S. SWINNEA, AND H. STEINFINK

Materials Science and Engineering, Department of Chemical Engineering, The University of Texas at Austin, Austin, Texas 78712

W. M. REIFF

Department of Chemistry, Northeastern University, Boston, Massachusetts 02115

AND S. PEI AND J. D. JORGENSEN

Argonne National Laboratory, Argonne, Illinois 60439

Received April 10, 1992; in revised form June 22, 1992; accepted June 25, 1992

Single-crystal X-ray diffraction and neutron powder diffraction analyses were employed to study the reversible intercalation of oxygen in the phase $LaSr_3Fe_3O_{10-\delta}$ and in the mixed Fe/Al analogue. A single-crystal X-ray diffraction study was done on $LaSr_3(Fe_{0.8}Al_{0.2})_3O_{8.95}$, M_r = 695.18, tetragonal, *I4/mmm*, a = 3.8665(8) Å, c = 28.369(4) Å, V = 424.1(2) Å^3, Z = 2, D_x = 5.44 g cm^{-3}, Mo$K\alpha$ = 0.71069 Å, μ = 272.1 cm^{-1}, $F(000)$ = 625.6, R = 0.025 for 227 reflections with $F > 5\sigma(F)$. The crystal structure consists of a triple layer of octahedra separated by La/Sr–O layers. The oxygen stoichiometry is variable and Rietveld refinement of neutron powder diffraction data in addition to the X-ray study was used to determine the vacancy sites. The vacancies occur primarily in the equatorial layer of the central octahedron. The value of the c-axis parameter is a linear function of the oxygen stoichiometry and increases with decreasing oxygen content. It varies from 28.04 Å for the phase $LaSr_3Fe_3O_{9.9}$ to 28.52 Å for the phase containing 9.2 oxygen atoms. The range of the c-axis variation is narrower for the Al-containing phase than for the pure Fe compounds. It ranges from about 28.1 Å for $LaSr_3Fe_{2.4}Al_{0.6}O_{9.3}$ to 28.4 Å for the phase containing about 8.9 oxygen atoms. Intercalation of oxygen occurs reversibly as a function of temperature. A given oxygen stoichiometry can be obtained by quenching the material from an elevated temperature into liquid nitrogen. The thermal displacement parameter of the cation occupying the central octahedron increases in the (001) plane with increasing oxygen deficiency in the equatorial layer of this octahedron. This displacement is interpreted as motion of the cation into a tetrahedral coordination environment. The range of oxygen stoichiometry for $LaSr_3Fe_3O_{10-\delta}$ is $0.1 \leq \delta \leq 0.8$; for the Al-containing phase it is $0.65 \leq \delta \leq 1.1$. Single-phase material can be synthesized with La, Nd, Pr, and Gd but not with Er. No substitution of Sr by Ba or Ca was possible. The solid solution range $Sr_{4-x}La_x$ is very narrow, $0.96 \leq x \leq 1.04$. Ferromagnetic and antiferromagnetic exchange interactions are present in $LaSr_3Fe_3O_{10-\delta}$; the former predominates at small values of δ and the latter when δ becomes large.

0022-4596/93 $5.00

Introduction

Intergrowth crystal structures in inorganic systems have provided a fertile field of solid state chemical research for many years, and the discovery of high-T_c superconducting cuprates has focused attention on intergrowth structures based on perovskite blocks. Aurivillius (*1–3*) described the preparation and crystal structures of a series of compounds in which layers formed by two or more sequences of perovskite units are separated by Bi_2O_2 layers. The octahedral interstices of the perovskite units are occupied by transition metals such as Ti, Nb, and Ta, and the dodecahedral interstices by alkaline earth ions. Ruddlesden and Popper (R-P hereafter) (*4*) have described intergrowth structures with the general formula $Sr_{n+1}Ti_nO_{3n+1}$, where n is the number of perovskite layers that, in turn, are separated by SrO halite layers. Indeed, La_2CuO_4 corresponds to the $n = 1$ phase and $(La_{2-x}Sr_x)CuO_{4\pm\delta}$, which initiated the revolutionary discovery of high-T_c superconducting cuprates, has this structure.

Numerous structures have been derived from the R-P parent compounds by the replacement of Ti^{4+} with lower valent transition metals and charge compensation by higher valent ions on the alkaline earth site. Thus the series of compounds $Ln_2AM_2O_7$, Ln^{3+} = La, Nd, Sm, Eu, Gd, or Tb, A^{2+} = Sr or Ba, M^{3+} = Mn or Fe, has been synthesized (*5, 6*). The replacement of Ti^{4+} by Cu^{2+} to form $La_2SrCu_2O_6$ requires the removal of an oxygen ion for overall charge neutrality. The apical oxygen joining the two octahedra is missing, resulting in layers of copper pyramids whose bases face each other (*7*), reminiscent of the cuprate layers in $YBa_2Cu_3O_7$. Thus the lowering of the valence of the octahedral ion from 4+ to 3+ is charge compensated by trivalent rare earth ions and maintains the octahedral double layer. However, the replacement of the 4+ ion by Cu^{2+} introduces a modification in the structure by the removal of the apical O^{2-} ion to create separate copper pyramids. The replacement of $2Ti^{4+}$ in the parent compound with $n = 2$ by $Fe^{3+}Cu^{2+}$ again causes the removal of an oxygen ion, but now the unshared apex of the octahedron is lost. The structure of $YBaFeCuO_5$ contains double layers of apex-sharing Fe/Cu pyramids separated by a single layer of Y in eightfold coordination—a fluorite unit (*8*). In $Y_2Sr FeCuO_{6.5}$ the structure consists also of the apex-sharing Fe/Cu pyramids but they are separated by a double layer of defect fluorite units consisting of Y in sevenfold coordination (*9*).

Compounds based on the parent structure with $n = 3$, $Sr_4Ti_3O_{10}$, have not been investigated extensively. Brisi and Rolando (*10*) studied the system Sr–Fe–O and report an oxygen deficient $Sr_4Fe_3O_{10-x}$. The compounds $Ba_4Pb_3O_{10}$ (*11*) and $Ba_4In_3O_{8.5}$ (*12*) have been synthesized and the latter contains oxygen vacancies to charge compensate for the substitution of In^{3+} for a tetravalent ion. A detailed redetermination of the structures of several Ca–Ti and Sr–Ti R-P phases has recently been published (*13*). The syntheses and physical properties of compounds $Sr_{n+1}V_nO_{3n+1}$ (n = 2,3) have been reported and the influence of oxygen deficiencies on the electrical and magnetic behavior investigated (*14–17*). We decided to investigate the crystal chemistry of $LaSr_3Fe_3O_{10-\delta}$ because charge compensation can occur by oxygen vacancy formation as well as by the variable valence of Fe.

Experimental

X-Ray Structure Analysis

A mixture consisting of $1La_2O_3$: $2SrCO_3$: 2CuO: $1Fe_2O_3$ with 10 wt% Bi_2O_3 as a flux was placed in an alumina boat and heated at 1130°C for 24 hr, 1125°C for 12 hr, and 1110°C for 12 hr, and furnace cooled to 600°C before the sample was removed. Single crystals had grown at the zone in which

the mixture was in contact with the walls of the boat. Several crystals were removed and analyzed by standardless energy dispersive X-ray fluorescence analysis (EDX). Surprisingly, these crystals contained a significant amount of Al, but only about 3% Cu; the ratio of (La, Sr) : (Fe, Al) was close to 4 : 3. Weissenberg and precession diagrams showed that the crystals were tetragonal, *I4/mmm*, a = 3.86 Å, c = 28.2 Å. These parameters are consistent with a structure containing three octahedra bridged by apical oxygens as found in $Sr_4Ti_3O_{10}$ (*4*).

A single crystal was selected and mounted on a Krisel automated Picker diffractometer equipped with an incident-beam graphite monochromator. The data collection, data reduction, and least-squares refinement results are summarized in Table I.

The lattice constants were obtained from a least-squares calculation of precisely determined 2θ values of the eight equivalent reflections for 12 separate reflections in the 2θ range 25°–27°. The variations in the intensities of the four standard reflections measured after every 180 min decreased at a constant rate with time and the intensities were corrected by the use of the equation $I = 1 - 0.002t$, t in hr. The corrections were less than ±2%. Estimated standard deviations, $\sigma(F_0)$, were obtained from counting statistics. Absorption corrections were calculated using ORABS (*18*); direct-methods calculations and least-squares refinements were carried out with SHELX 76 (*19*). The atomic scattering factors for neutral atoms and corrections for anomalous dispersion were obtained from the "International Tables for X-ray Crystallography" (*20*). An extinction correction, g, was applied using the expression $F'_{calc} = F_{calc}(1 - gF^2/\sin\theta)$.

An E-map showed that the cation positions were consistent with the structure proposed by R-P for n = 3 (*4*). Least-squares refinement using Sr and Fe and isotropic temperature factors converged to R = 0.127. A Fourier electron density map revealed the oxygen positions and their inclusion in the refinement caused it to converge to R = 0.09. The introduction of La into the two crystallographically independent Sr sites with variable occupancies decreased R to 0.05 and indicated a La : Sr ratio of 1 : 3 in each site. Synthesis of polycrystalline samples of this phase using this ratio of La : Sr yielded single-phase material. Thereafter the occupancy of each site in the single-crystal least-squares refinements was fixed at that ratio. The weighted least-squares refinement with anisotropic thermal displacement parameters for the cations, the vari-

TABLE I

SUMMARY OF DATA COLLECTION AND STRUCTURE REFINEMENT FOR $LaSr_3(Fe_{0.8}Al_{0.2})_3O_{8.95}$

Formula weight	695.18
Crystal system	Tetragonal
a, Å	3.8665(8)
c, Å	28.369(4)
V, Å^3	424.1(2)
Space group	I4/mmm
Z	2
D_x(g cm^{-3})	5.44
μ(cm^{-1})	272.1
λ(Å)	0.71069
F(000)	625.6
Dimensions (μm)	220 × 120 × 130
Mode	$\theta - 2\theta$
Max. 2θ	60°
Scan rate (deg min^{-1})	variable, $\sigma(I)/I = 0.02$
Scan width	$2 + 0.70 \tan\theta$
hkl min	−5, −5, 0
hkl max	5, 5, 39
Reflections, measured	1278
Reflections, unique	240
R_{int}	0.021
$\geq 5\,\sigma(F)$	227
Transmission factor	0.699 – 0.137
Standard reflections	217, $\bar{2}17$, 114, $\bar{1}14$
Number of variables	26
w^{-1}	$\sigma^2(F_0) + 0.00002\,F_0^2$
Goodness of fit, S	2.48
Function minimized	$\Sigma w(\|Fo\| - \|Fc\|)^2$
R, wR	0.025, 0.025
max shift/e.s.d.	0.003
$\Delta\rho$, max, min (e Å^{-3})	1.76, 1.11
g, extinction	$5(1) \times 10^{-8}$

able Fe–Al occupancies in the crystallographic sites, and the inclusion of an extinction correction converged to $R = 0.0252$. The very small amount of Cu present in this crystal was not separately included in the refinement. The use of only Fe contributions to the scattered intensity from the octahedral site occupants yielded less than full occupancy. The addition of Al in those sites converged to an Fe : Al ratio consistent with the EDX determination.

The synthesis of $LaSr_3Fe_3O_x$ from a starting composition $0.5La_2O_3 : 3SrO : 1.5Fe_2O_3$ yielded single phase material showing that neither Cu nor Al are necessary for the formation of this phase. The final parameters resulting from the X-ray data refinement are shown in Table II and a table of F_0, F_c, and $\sigma(F_0)$ has been deposited.[1]

Neutron Powder Diffraction Analysis

Structures of four samples, (1) $LaSr_3Fe_3O_{10-\delta}$ annealed in 200 atm O_2 at 400°C, (2) $LaSr_3Fe_3O_{10-\delta}$ quenched from 800°C into liquid N_2, (3) $LaSr_3(Fe_{0.8},Al_{0.2})_3O_{10-\delta}$ furnace cooled in air, and (4) $LaSr_3(Fe_{0.8},Al_{0.2})_3O_{10-\delta}$ quenched from 600°C into liquid N_2, were studied by neutron powder diffraction. The time-of-flight data were collected using the General Purpose Powder Diffractometer (GPPD) at Argonne's Intense Pulsed Neutron Source (*21*). Although the data were collected simultaneously at several angles, only the high-resolution back-scattering data ($2\theta = 148°$) were used for full structural analyses by Rietveld refinement (*22*). The initial refinements were done using a single *I4/mmm* model, with starting structural parameters taken from $Ba_4In_3O_{8.5}$ (*12*). A total of 598 reflections covering a *d*-spacing range from 0.5 to 2.8 Å was included in each refinement. This model yields satisfactory fits for the data taken from samples 1, 3, and 4. Figure 1 shows the Rietveld refinement profile for Sample 1. We note that Bragg peaks with strong *l* character were fit relatively poorly compared with other peaks. Such discrepancies could result from the occurrence of some stacking faults in this layered structure due to a long *c*-axis periodicity. On the other hand, the single-phase model yields a poor fit for the data obtained from sample 2. In plots of refined data for sample 2, we observed systematic appearances of distinct shoulders on Bragg peaks with strong *l* character. Since the *c*-axis parameter in this crystal structure changes substantially with oxygen content, we suspect that the shoulders are caused by oxygen inhomogeneity in the sample. Thus, the Rietveld refinement for sample 2 was repeated using two tetragonal *I4/mmm* phases with different lattice parameters, $a_1 = 3.868$ Å, $c = 28.255$ Å (75.4% by volume) and $a_2 = 3.870$ Å, $c_2 = 28.409$ Å (24.6% by volume) for an overall oxygen content of 9.50 (see Fig. 5). This two-phase model provided a satisfactory fit. The refined structural parameters for the four materials are listed in Table III. The bond lengths and angles are listed in Table IV.

Thermogravimetric Analysis, Mössbauer Spectroscopy, Magnetic Susceptibility

Thermogravimetric analysis was carried out with a Perkin–Elmer TGA-7 system. Mössbauer spectra were obtained on a conventional constant acceleration spectrometer operated in conjunction with a Canberra Series 35 multichannel analyzer, by using a 100-mCi ^{57}Co in rhodium metal matrix γ-ray source. Temperature control was achieved

[1] See NAPS document No. 04961 for 3 pages of supplementary materials. Order from ASIS/NAPS, Microfiche Publications, P.O. Box 3513, Grand Central Station, New York, NY 10163-3513. Remit in advance $4.00 for microfiche copy or for photocopy, $7.75 up to 20 pages plus $.30 for each additional page. All orders must be prepaid. Institutions and Organizations may order by purchase order. However, there is a billing and handling charge for this service of $15. Foreign orders add $4.50 for postage and handling, for the first 20 pages, and $1.00 for additional 10 pages of material, $1.50 for postage of any microfiche orders.

TABLE II

POSITIONAL AND THERMAL DISPLACEMENT PARAMETERS (Å^2)[a] FOR $LaSr_3(Fe_{0.8}Al_{0.2})_3O_{8.95}$ FROM X-RAY DIFFRACTION DATA

Atom	Occupancy	Site	x	y	z	$U_{11} = U_{22}$	U_{33}	B_{eq}[b]
Fe1	0.72(2)	2a	0	0	0	0.0165(9)	0.0078(3)	1.07(4)
Al1	0.27							
Fe2	0.83(1)	4e	0	0	0.14018(5)	0.0039(5)	0.0146(9)	0.59(3)
Al2	0.17							
($\frac{1}{4}$La,$\frac{3}{4}$Sr)1	1	4e	0	0	0.57247(3)	0.0151(3)	0.0142(5)	1.17(2)
($\frac{1}{4}$La,$\frac{3}{4}$Sr)2	1	4e	0	0	0.70133(3)	0.0083(3)	0.0081(4)	0.66(2)
O1	1	8g	0	$\frac{1}{2}$	0.1377(2)	0.0130(15)		1.03(12)
O2	0.88(3)	4e	0	0	0.0663(4)	0.033(3)		2.61(24)
O3	1	4e	0	0	0.2128(3)	0.022(2)		1.74(16)
O4	0.71(4)	4c	0	$\frac{1}{2}$	0	0.060(8)		4.7(6)

[a] The form of the anisotropic displacement parameter is $\exp\{-2\pi^2(U_{11}a^{*2}h^2 + \ldots + 2\,U_{23}b^*c^*kl + \ldots)\}$. U_{11} and U_{33} are the nonzero coefficients.

[b] $U_{eq} = \frac{1}{3}$(trace) of the diagonalized tensor. $B_{eq} = 8\pi^2U_{eq}$.

by using an uncalibrated silicon diode coupled to a Lake Shore Cryotronics model DT-500 C set point controller. Temperature measurements were made with a digital voltmeter by using a calibrated silicon diode driven by a 10-μA constant current source. Spectra below room temperature were obtained by using either a flow-type or an ex-

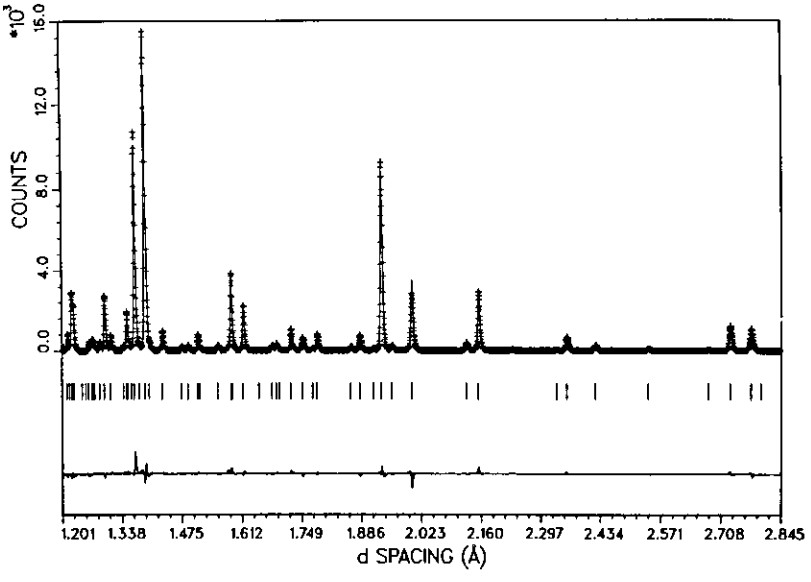

FIG. 1. Portion of the Rietveld refinement profile for $LaSr_3Fe_3O_{9.88}$ at room temperature. Plus marks (+) are the raw data; the solid line is the calculated profile. Tick marks below the profile mark the positions of allowed reflections. A difference curve (observed–calculated) is plotted beneath.

TABLE III

POSITIONAL AND THERMAL DISPLACEMENT PARAMETERS FROM RIETVELD REFINEMENT OF POWDER NEUTRON DIFFRACTION DATA FOR $LaSr_3Fe_3O_{10-\delta}$ AND $LaSr_3(Fe_{1-x}Al_x)_3O_{10-\delta}$

Atom	Occupancy	Site	x	y	z	B_{iso} (Å^2)
			$LaSr_3Fe_3O_{9.88}$			
Fe1	1	2*a*	0	0	0	0.55(4)
Fe2	1	4*e*	0	0	0.1392(1)	0.71(3)
($\frac{1}{4}$La/$\frac{3}{4}$Sr)1	1	4*e*	0	0	0.5690(1)	0.80(3)
($\frac{1}{4}$La/$\frac{3}{4}$Sr)2	1	4*e*	0	0	0.7013(1)	0.70(4)
O1	1.000(7)	8*g*	0	$\frac{1}{2}$	0.1382(1)	1.02(5)
O2	0.97(1)	4*e*	0	0	0.0690(1)	0.96(6)
O3	1.01(1)	4*e*	0	0	0.2110(1)	1.35(8)
O4	0.97(1)	4*c*	0	$\frac{1}{2}$	0	0.92(8)
			$LaSr_3Fe_3O_{9.45}$			
Fe1	1	2*a*	0	0	0	0.81(4)
Fe2	1	4*e*	0	0	0.1411(1)	0.67(3)
($\frac{1}{4}$La/$\frac{3}{4}$Sr)1	1	4*e*	0	0	0.5708(1)	0.72(3)
($\frac{1}{4}$La/$\frac{3}{4}$Sr)2	1	4*e*	0	0	0.7011(1)	0.87(4)
O1	0.995(8)	8*g*	0	$\frac{1}{2}$	0.1380(1)	0.90(4)
O2	0.95(1)	4*e*	0	0	0.0658(1)	1.7(1)
O3	1.03(2)	4*e*	0	0	0.2114(1)	1.8(1)
O4	0.79(2)	4*c*	0	$\frac{1}{2}$	0	3.1(2)
			$LaSr_3(Fe_{0.86},Al_{0.14})_3O_{9.28}$			
Fe1	0.72(1)	2*a*	0	0	0	0.65(6)
Al1	0.28	2*a*	0	0	0	0.65
Fe2	0.93(1)	4*e*	0	0	0.1403(1)	0.61(3)
Al2	0.07	4*e*	0	0	0.1403	0.61
($\frac{1}{4}$La/$\frac{3}{4}$Sr)1	1	4*e*	0	0	0.5703(1)	0.93(4)
($\frac{1}{4}$La/$\frac{3}{4}$Sr)2	1	4*e*	0	0	0.7013(1)	0.84(4)
O1	0.984(9)	8*g*	0	$\frac{1}{2}$	0.1377(1)	0.80(3)
O2	0.88(1)	4*e*	0	0	0.0671(1)	1.41(8)
O3	0.98(1)	4*e*	0	0	0.2113(1)	1.36(7)
O4	0.81(2)	4*c*	0	$\frac{1}{2}$	0	2.4(1)
			$LaSr_3(Fe_{0.85},Al_{0.15})_3O_{9.05}$			
Fe1	0.70(1)	2*a*	0	0	0	0.92(6)
Al1	0.30	2*a*	0	0	0	0.92
Fe2	0.92(1)	4*e*	0	0	0.14122(5)	0.61(3)
Al2	0.08	4*e*	0	0	0.14122	0.61
($\frac{1}{4}$La/$\frac{3}{4}$Sr)1	1	4*e*	0	0	0.57186(8)	0.94(4)
($\frac{1}{4}$La/$\frac{3}{4}$Sr)2	1	4*e*	0	0	0.70158(6)	0.85(4)
O1	0.99(1)	8*g*	0	$\frac{1}{2}$	0.13768(7)	0.82(3)
O2	0.85(1)	4*e*	0	0	0.0655(1)	1.81(9)
O3	0.98(1)	4*e*	0	0	0.21185(9)	1.43(7)
O4	0.72(2)	4*c*	0	$\frac{1}{2}$	0	3.9(2)

change-type Janis cryostat in either a horizontal or a vertical mode. Isomer shifts are relative to metallic Fe at room temperature. Magnetic susceptibilities were measured with a Quantum Design Co. 5000 DC SQUID magnetometer between room temperature and 10 K. The applied magnetic field was 1000 G. About 400–500 mg of sam-

TABLE IV

BOND LENGTHS (Å) AND ANGLES (deg) RESULTING FROM RIETVELD REFINEMENT OF POWDER NEUTRON DIFFRACTION DATA AND FROM A SINGLE CRYSTAL X-RAY DIFFRACTION LEAST-SQUARES REFINEMENT

	Neutron				X-ray
	$LaSr_3Fe_3O_{9.88}$	$LaSr_3Fe_3O_{9.45}$	$LaSr_3(Fe_{0.86}Al_{0.14})_3O_{9.28}$	$LaSr_3(Fe_{0.85}Al_{0.15})_3O_{9.05}$	$LaSr_3(Fe_{0.8}Al_{0.2})_3O_{8.95}$
			Bond length		
(Fe/Al)1–O2 ×2	1.935(3)	1.857(5)	1.889(3)	1.8545(1)	1.8794(3)
–O4 ×4	1.9331(1)	1.9343(1)	1.9297(1)	1.9321(1)	1.9333(4)
(Fe/Al)2–O1 ×4	1.9333(1)	1.9360(1)	1.9311(1)	1.9347(1)	1.9345(4)
–O2	1.968(3)	2.129(6)	2.063(3)	2.1438(1)	2.0973(3)
–O3	2.015(3)	1.991(5)	1.999(3)	1.9997(1)	2.0596(3)
(La/Sr)1–O1 ×4	2.739(2)	2.718(3)	2.707(2)	2.6843(1)	2.6760(3)
–O2 ×4	2.7339(1)	2.7389(3)	2.7305(1)	2.7383(1)	2.7397(6)
–O4 ×4	2.734(2)	2.778(2)	2.765(2)	2.8057(1)	2.8221(4)
(La/Sr)2–O1 ×4	2.622(2)	2.630(3)	2.632(2)	2.6469(1)	2.6452(3)
–O3 ×4	2.7474(3)	2.7510(5)	2.7436(3)	2.7477(1)	2.7533(6)
–O3	2.458(3)	2.472(5)	2.461(3)	2.4510(1)	2.4366(3)
O1–O1 ×4	2.7339(1)	2.7355(1)	2.7290(1)	2.7323(1)	2.7340(6)
–O2 ×2	2.739(2)	2.816(4)	2.772(3)	2.8121(1)	2.8009(3)
–O3 ×2	2.813(2)	2.836(4)	2.831(2)	2.8535(1)	2.8767(4)
O2–O4 ×4	2.735(2)	2.681(4)	2.700(2)	2.6780(1)	2.6963(3)
O4–O4 ×4	2.7339(1)	2.7355(1)	2.7290(1)	2.7323(1)	2.7340(6)
			Bond angle		
O1–Fe2–O1	178.3(2)	175.1(2)	175.7(2)	174.06(1)	175.8(3)
O1–Fe2–O1	89.16(8)	87.56(10)	87.84(7)	87.03(1)	87.91(15)
O1–Fe2–O1	90.84(8)	92.44(10)	92.16(7)	92.97(1)	92.09(15)

ple were used in the measurements. Diamagnetic corrections were not applied because they were too small.

Results

The crystal structure of this compound is illustrated in Fig. 2. It consists of layers of FeO_6 octahedra perpendicular to the *c*-axis. The apical oxygen atoms of the central octahedron are shared by an octahedron above and below and form a slab 12.1 Å high parallel to the *c*-axis. The octahedra articulate laterally by corner sharing of oxygen atoms. The triple perovskite layers are separated by La/Sr–O rock-salt units in agreement with the structure proposed by R-P (*4*).

The bond lengths and angles from the neutron and X-ray refinements are shown in Table IV. The equatorial *M*1–O4 (*M* = Fe, Fe/Al) bond lengths for the central octahedra are nearly equal, with an average value for the five phases of 1.933(2) Å. The apical *M*1–O2 bond lengths are significantly shorter than the equatorial values and strongly depend on oxygen stoichiometry. The *M*2–O2 bond lengths are significantly longer than *M*1–O2 and also depend on the oxygen stoichiometry. The average equatorial bond length *M*2–O1 is 1.934(2) Å, the same as for the central octahedron, and the average *M*2–O3 bond length to the unshared apex is 2.01(3) Å. One La/Sr is in a dodecahedral site with an average oxygen bond length of 2.74(4) Å and the other crystallographically independent La/Sr is in ninefold coordination, a monocapped square antiprism, with oxygen bond distances varying from 2.4366(3) to 2.7510(5) Å.

The oxygen content of these phases is

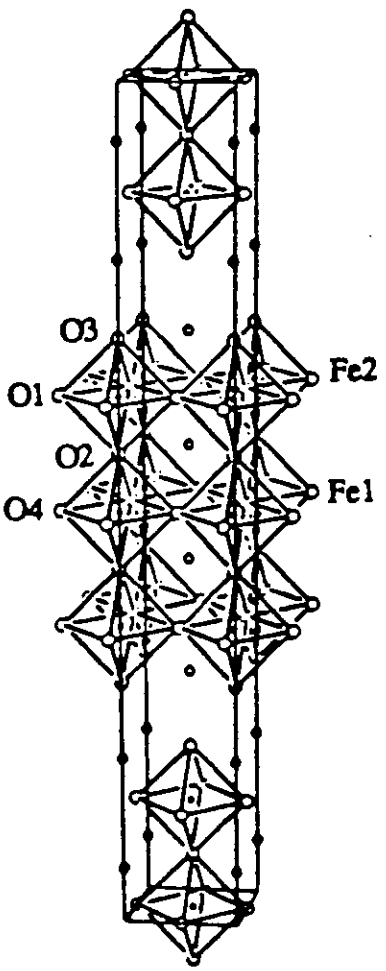

FIG. 2. The crystal structure of $LaSr_3Fe_3O_{10}$. Open circles connected by bonds are oxygen; solid circles within the octahedra are Fe; nonbonded open circles are La/Sr. The oxygen levels are labeled.

variable. The O1 and O3 sites are fully occupied; they are, respectively, the equatorial and unshared apical oxygen atoms of the $M2$ octahedron. The oxygen vacancies occur in the O2 and O4 sites that form the octahedron around the central unit occupied by $M1$. Results of neutron powder diffraction refinements show that the $LaSr_3Fe_3O_{10-\delta}$ material annealed at 200 atm O_2 is essentially stoichiometric in oxygen content, 9.88(6). However, small amounts of oxygen vacancies on the O2 and O4 sites are present, see Table III. Due to similar scattering lengths for La (0.827×10^{-12} cm) and Sr (0.702×10^{-12} cm), the composition ratio of La to Sr was not refined and was fixed at the known composition. Refinements for sample 2 using two tetragonal phases show that the majority of the sample, about 80%, has an oxygen content of 9.45(8). The rest of the sample has a slightly lower oxygen content, causing the c-axis to expand slightly and resulting in shoulders on some Bragg reflections. The difference of the refined oxygen contents between samples 1 and 2 is about 0.43, which is consistent with the thermogravimetric analysis (TGA) result of 0.4. The Al-doped material, sample 4, has an oxygen deficiency close to that of the single crystal on which X-ray data were collected. Agreement among the parameters is good with the notable exception of the Al content in position $M2$.

The TGA of $LaSr_3Fe_3O_{10-\delta}$ and $LaSr_3(Fe_{3-x}Al_x)O_{10-\delta}$ shows that oxygen is reversibly lost and reintercalated, Figs. 3a and 3b. The oxygen-deficient starting material is prepared by quenching the fully oxidized phase from a given temperature into liquid N_2. Initial oxygen sorption begins at 200°C, reaches its maximum at about 350°C, and thereafter oxygen is lost continuously to 900°C. Cooling in air reversibly intercalates oxygen with the final composition reaching $O_{9.9}$. The variations of oxygen stoichiometry in air with temperature for the Fe and Fe/Al phases are shown in Fig. 4. Samples of the fully oxygenated Fe phase were quenched into liquid N_2 from 500 to 1000°C in intervals of 100°C after the samples were held at the respective temperatures for at least 4 hr. X-ray diffraction patterns were immediately obtained from the quenched samples. The powder patterns showed a strong c-axis parameter dependence on the oxygen content, increasing in value with decreasing oxygen content. When the

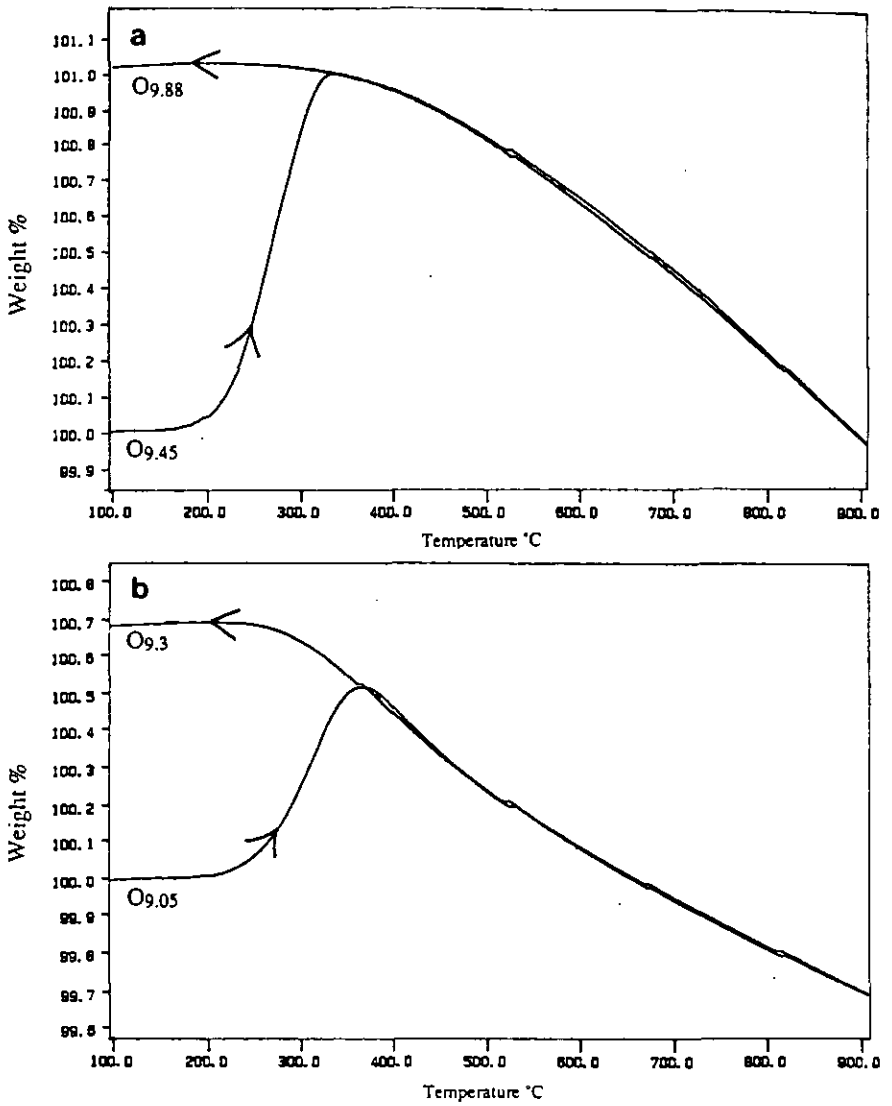

FIG. 3. Thermogravimetric curves in air for (a) $LaSr_3Fe_3O_{10-\delta}$ and (b) $LaSr_3Fe_{2.40}Al_{0.60}O_{10-\delta}$.

quenched material is exposed to the ambient laboratory atmosphere for 1 day or longer the powder X-ray diffraction pattern contains a significant amount of a cubic second phase. The kinetics of the decomposition depends on the oxygen content of the quenched phase. The greater the oxygen deficiency of the sample, the faster its decomposition.

Specimens with the composition $LaSr_3Fe_{2.6}Al_{0.4}O_{10-\delta}$ were quenched from 600 and 800°C. The *c*-axis parameter as a function of temperature, Fig. 4, also increases with loss of oxygen, although the *c*-axis is smaller than for the Al-free phase for a given oxygen stoichiometry. The presence of Al in the Fe site stabilizes an oxygen deficient phase and causes the oxygen content to vary over a

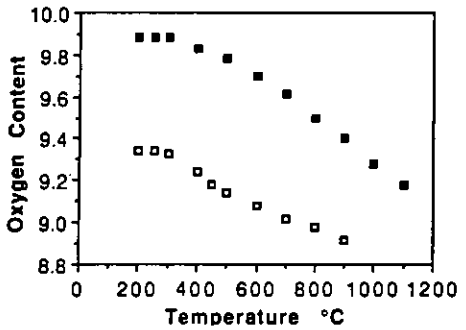

FIG. 4. The variation of oxygen stoichiometry with temperature for the Fe (filled squares) and Fe/Al (open squares) phases.

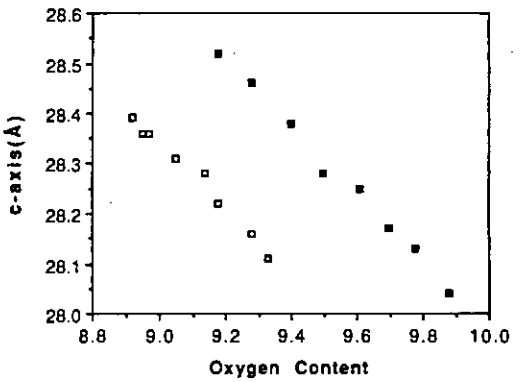

FIG. 5. The variation of the *c*-axis with oxygen stoichiometry for the Fe (filled squares) and Fe/Al (open squares) phases.

much narrower range than for the pure Fe phase.

Discussion

The oxygen vacancies occur primarily in the O4 and O2 sites that constitute the octahedral coordination around the central cation, *M*1. The vacancies in the structure of $Ba_4In_3O_{8.5}$ ($Ba_8In_6O_{17}$) occur in the same sites (*12*). In $LaSr_3Fe_3O_{9.88}$ the two Fe1–O2 apical bond lengths are 1.935(3) Å, comparable with the four equatorial bond lengths of Fe1–O4, 1.9331(1) Å, so that for a fully oxygenated compound the octahedron is regular. In the oxygen deficient 9.45 phase the apical Fe1–O2 bond lengths shorten to 1.875(5) Å while the four equatorial Fe1–O4 bond lengths remain essentailly unchanged at 1.9343(1) Å. The distal octahedron is distorted. In the 9.88 phase the four equatorial Fe2–O1 bonds are 1.9333(1) Å, the same as for the central octahedron, but the bridging Fe2–O2 bond is 1.968(3) Å and the bond to the nonbridging O3 is 2.015(3) Å. In the oxygen 9.45 phase the equatorial bonds remain unchanged, but the bridging Fe2–O2 bond lengthens considerably to 2.129(6) Å while the nonbridging Fe2–O3 contracts slightly to 1.991(5) Å; an overall expansion parallel to the *c*-axis of about 1%. The X-ray diffraction patterns of polycrystalline samples of $LaSr_3Fe_3O_{10-\delta}$ heated and quenched into liquid N_2 provide a linear relationship between the *c*-axis dimension and oxygen content, Fig. 5. In Table V the lattice parameters for all phases that were refined by Rietveld and least-squares analyses are summarized.

Similar behavior is seen for the $LaSr_3(Fe_{0.8}Al_{0.2})_3O_{10-\delta}$ phases. The highest vacancy concentrations occur in the O4 position; the O2 bridging position has a slight and constant vacancy concentration. The variation of (Fe/Al)1–O2 apical bonds is not as pronounced as for the pure Fe compound, and lengthening of the (Fe/Al)2–O2 bond occurs with decreasing oxygen content. The

TABLE V

LATTICE PARAMETERS OF PHASES WHOSE OXYGEN STOICHIOMETRY IS BASED ON NEUTRON AND X-RAY DIFFRACTION DATA REFINEMENTS

	a, Å	*c*, Å
$LaSr_3Fe_3O_{9.88}$	3.8663(1)	28.0407(3)
$LaSr_3Fe_3O_{9.45}$	3.8677(1)	28.2553(5)
$LaSr_3(Fe_{0.86}Al_{0.14})_3O_{9.28}$	3.8594(1)	28.1579(3)
$LaSr_3(Fe_{0.85}Al_{0.15})_3O_{9.05}$	3.8641(1)	28.3124(3)
$LaSr_3(Fe_{0.8}Al_{0.2})O_{8.95}$	3.8665(8)	28.369(4)

agreement between the single-crystal X-ray diffraction results and the neutron powder diffraction results is generally good with one notable exception. The Al substitution in the Fe1 (central octahedron site) is 0.28 according to the X-ray data and 0.30 according to the neutron data. The Al content in the Fe2 site is 0.17 (X-ray) and 0.08 (neutron). The *c*-axis variation as a function of oxygen content is also linear with the same slope as for the pure Fe phase but the *c*-axis parameters are slightly lower.

The thermal displacement parameters of the two crystallographically distinct octahedral cation positions are noteworthy. The neutron diffraction refinement for the pure Fe compound shows that the isotropic B parameter of Fe1 for the fully oxygenated phase is 0.55(4) Å^2, and it becomes 0.81(4) Å^2 for the 9.45 phase. The Fe2 values remain constant at about 0.7 Å^2. The neutron data for the Fe/Al compound yields an isotropic value of 0.65(6) Å^2 for the 9.3 phase (maximum oxygen content) and 0.92(6) Å^2 for the 9.05 phase. The parameter for (Fe/Al)2 remains constant at 0.61(3) Å^2. The X-ray data yielded anisotropic displacement parameters for the 8.95 phase of $B_{11} = B_{22} = 1.30(7)$ Å^2, $B_{33} = 0.61(10)$ Å^2 for the central octahedron cation, $(Fe_{0.72}Al_{0.28})1$, and $B_{11} = B_{22} = 0.31(4)$ Å^2, $B_{33} = 1.16(6)$ Å^2 for the distal octahedron site, $(Fe_{0.83}Al_{0.17})2$. We interpret these observations in terms of positional displacements rather than thermal displacements. As the O4 sites become depleted, the central octahedral cation moves off the 000 position to assume a tetrahedral coordination. The bridging bond length shrinks toward the now "tetrahedral" site and the distal octahedral site–bridging oxygen, Fe2–O2, lengthens. The Al substitution occurs primarily in the central octahedron and increases the tendency toward a tetrahedral site environment. The hypothetical compound $LaSr_3Fe_2AlO_9$ presumably might have an articulation in which the two outside octahedral layers are connected by a tetrahedral layer. Such an O–T–O triple layer exists in the brownmillerite structure (*23*).

The anisotropically refined values of the thermal displacement parameters for the two crystallograhpically independent LaSr scatterers indicate that the displacement is isotropic. It is slightly larger for the dodecahedrally coordinated La/Sr1 than for La/Sr2 in ninefold coordination. The oxygen vacancies probably increase the effective hole radius of the dodecahedral interstice, permitting the cation occupant a larger vibrational amplitude than for the cation that is bonded only to the fully occupied oxygen ion sites, O3 and O1.

Bond–valence calculations (*24*) for the $O_{9.88}$ phase using the expression $V = \sum_i \exp((r_0 - r_i)/0.37)$, $r_0(Fe^{3+}) = 1.759$, r_0 $(\frac{1}{4}La^{3+} + \frac{3}{4}Sr^{2+}) = 2.132$, yield +3.92 for Fe1, +3.33 for Fe2, +2.28 for La/Sr1, and +2.20 for La/Sr2. The valence sums for La/Sr are equal to the weighted value for the site occupant in the structure. The valence sums for Fe may signify that both crystallographic sites become oxidized as oxygen content increases.

Magnetic susceptibilities as a function of temperature are shown in Fig. 6, yielding the effective moments and Weiss constants summarized in Table VI. The behavior is typical for that of a 2D antiferromagnet, displaying broad maxima that become less pronounced as the oxygen vacancies increase. The ordering temperature of about 200 K for the oxygen 9.88 phase drops to about 150 K for the 9.5 phase and is difficult to observe for the 9.1 phase. The onset temperature of 3D ordering as observed in Mössbauer spectra hyperfine splitting similarly decreases with oxygen content. The variation of oxygen content from 9, i.e., all trivalent iron, requires the appropriate changes in the oxidation state of iron for charge compensation. For formal charge balance the two crystallographically equivalent outer Fe2 atoms are expected to be tetravalent in $LaSr_3Fe_3O_{10}$, but valence–bond sum calcu-

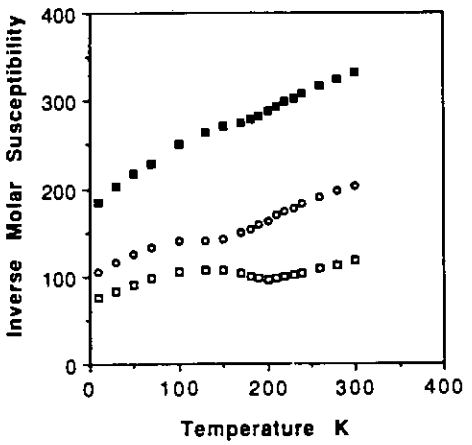

FIG. 6. The inverse magnetic susceptibility vs T for three different oxygen stoichiometries: $LaSr_3Fe_3O_{9.88}$, open squares; $LaSr_3Fe_3O_{9.45}$, open circles; and $LaSr_3Fe_3O_{9.05}$, filled squares.

lations indicate that both crystallographic sites are oxidized. No clear-cut evidence for Fe^{4+} is seen in the effective magnetic moment and, more importantly, in Mössbauer data. The observed isomer shifts ranging from +0.15 to +0.20 mm/sec relative to iron metal are reasonable for high-spin Fe(III) in a highly delocalized, covalent, six-coordinated, oxygen environment. Similarly coordinated actual Fe IV ions in $SrFeO_3$ have isomer shifts of about −0.15 mm/sec (*25*).

The room-temperature Mössbauer spectrum for $LaSr_3Fe_3O_{9.88}$ exhibits a broad, unresolved absorption band. The more resolved spectrum observed at 181.8 K, Fig. 7, can be decomposed into three lines, a quadrupole split pair originating from the Fe2 crystallographic site and a singlet from the central octahedral Fe1 site. The foregoing decomposition corresponds to a best fit for three independent Lorentzians. The association of a quadrupole doublet with the outer pair of peaks is logical in terms of the known structure and realistic isomer shift assignments. The spectrum obtained at 77 K from $LaSr_3(Fe_{0.8}Al_{0.2})_3O_{9.3}$, Fig. 8, at approximately twice the velocity sweep of Fig. 7, can similarly be decomposed into a three-line spectrum. At 4.8 K hyperfine splitting is observed. A small unresolved or zero quadrupole splitting effect is consistent with the more symmetric coordination of the Fe(1) crystallographic site. For both systems, the ratio of the intensity of site (2) : site (1) is about 1.1–1.2; i.e., less than the expected value of 2 : 1. This is explicable if the recoil free fraction of the Fe(2) sites is less than that of the Fe(1) sites. This will, in turn, result from weaker bonding at Fe(2) sites as suggested by the measurably longer F(2)–O axial bond lengths. In Table IV the differences in the Fe(1)–O(2) and O(2)–Fe(2)–O(3) bond lengths vary from about 0.06 to 0.2 Å. At 4.2 K two six-transition Zeeman patterns are observed, but again with an intensity ratio of about 1 rather than 2. Complete details of the Mössbauer spectra for a number of these phases will be published elsewhere (*26*).

TABLE VI

MAGNETIC PARAMETERS FOR $LaSr_3Fe_3O_x$

x	μ(eff), B.M.	θ, K
9.88	5.76	−185
9.5	4.66	−248
9.1	4.30	−464

The magnetic values in Table VI are strongly dependent on the number of data measured in the paramagnetic region. Usually the Curie–Weiss parameters are most reliably obtained from data measured at temperatures exceeding two or three times T_{max}. These compounds lose oxygen above room temperature and measurements were therefore restricted to 300 K and below. Therefore, the derived values of μ_{eff} and θ should be considered as indicative of a trend rather than as precise values. An inspection of Fig. 6 shows that the best straight line

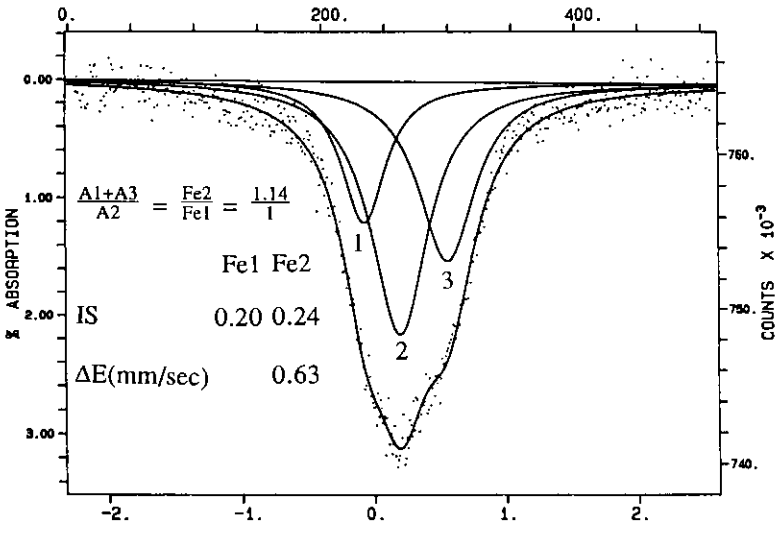

FIG. 7. Mössbauer spectrum of $LaSr_3Fe_3O_{9.88}$ at 181.8 K. The abscissa is in mm/sec relative to Fe.

can be fit to data obtained from the $x = 9.1$ phase. The slope of the best straight line to the $x = 9.5$ data set is essentially the same, although θ becomes less negative. A line with nearly the same slope can be drawn through the three highest temperature data points for the $x = 9.88$ phase, but θ now is even less negative. We interpret the change in the Weiss constant as due to competing antiferromagnetic and ferromagnetic exchange processes. The bond–valence calculations for the $O_{9.88}$ phase show that both crystallographic iron sites are oxidized beyond Fe^{3+}. Thus in the oxygenated phase the presence of Fe^{4+}–O–Fe^{3+} permits double exchange by fast hopping of an electron

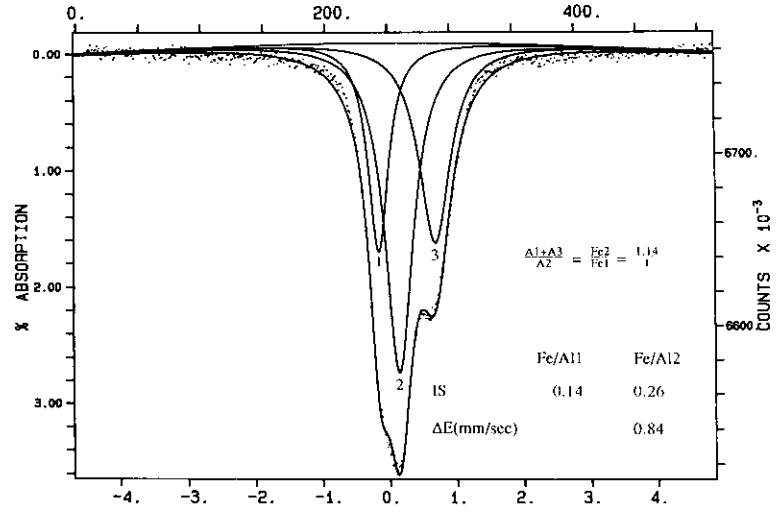

FIG. 8. Mössbauer spectrum of $LaSr_3Fe_{2.4}Al_{0.6}O_{9.3}$ at 77 K. The abscissa is in mm/sec relative to Fe.

among iron sites within the equatorial planes, causing parallel spin alignments; i.e., a ferromagnetic contribution to the susceptibility. The presence of a delocalized electron in such a covalently bonded system has been mentioned previously in the discussion of the Mössbauer results. The effective moment is also closest to the value for high-spin Fe^{3+}. In addition the presence of superexchange via the apical oxygen ions gives rise to an antiferromagnetic component. The assignment of the exchange paths is governed by the Fe–O bond lengths. They are shorter in the equatorial plane of the octahedron than to the apical oxygen ions. Oxygen is depleted primarily from the equatorial site of the central octahedron, O4; this cation site, Fe1, also contains the highest "Fe^{4+}" concentration. Thus as the oxygen content is depleted the ferromagnetic influence decreases, and this manifests itself by the increasingly negative value of the Weiss constant. The μ_{eff} values, Table VI, increase with increasing oxidation of iron in apparent contradiction to expectation for values based on noninteracting iron ions. As pointed out previously, no clear-cut evidence for localized Fe^{4+} is seen and since we postulate that the ferromagnetic exchange occurs laterally in the plane and is highest for the most oxidized phase the effective moment has the largest value. As the antiferromagnetic exchange becomes more important as oxygen is lost, the effective moment decreases. The behavior of Fe in a formal oxidation state greater than 3+ is a puzzling and vexing problem because of so many other influences that are present; e.g., electron delocalization and unequal cation–anion bond distances. The experimental observations reported here can be adequately explained by mechanisms that are at best only qualitative.

Attempts to synthesize $Sr_4Fe_3O_{10-\delta}$ (*10*) from mixtures of $SrCO_3$ and Fe_2O_3 were unsuccessful. Reaction temperatures of 1000 to 1450°C yielded cubic $SrFeO_{3-\delta}$, tetragonal $Sr_2Fe_2O_5$, and a small amount of an additional, unidentified component. Experiments using solutions of stoichiometric amounts of $Sr(NO_3)_2$ and $Fe(NO_3)_3 \cdot 9H_2O$, evaporated to dryness and fired at 750°C, yielded $Sr_4Fe_3O_{10-\delta}$ admixed with $SrFeO_{3-\delta}$ and a minor phase $Sr_3Fe_2O_{7-\delta}$. The product was poorly crystalline material. These results agree with those reported by Brisi and Rolando (*10*). Reaction temperatures below 750°C do not give rise to product formation; temperatures at or above 800°C do not produce $Sr_4Fe_3O_{10-\delta}$ but form $SrFeO_4$ and $Sr_3Fe_2O_{7-\delta}$.

The thermodynamic stability of $Sr_4Fe_3O_{10-\delta}$ is greatly enhanced by rare earth substitution for Sr. Mixtures of the respective oxides to yield the phase $LaSr_3Fe_3O_x$, when reacted at 1450°C, furnace cooled to 400°C in air, held at that temperature for 24 hr, and quenched, yielded a single-phase product. The oxygen content of the product depends on the quenching temperature. Single-phase material was observed for $LaSr_3Fe_3O_{10-\delta}$ for $0.1 \leq \delta \leq 0.8$ and for the Al-containing phase of $0.65 \leq \delta \leq 1.1$. Single-phase material can be synthesized with La, Nd, Pr, and Gd by reacting the appropriate mixtures of oxides at 1450°C in air. It was not possible to form this compound with Er. The solid solution range $Sr_{4-x}La_x$ was investigated and was, within the limits of second-phase detectability for the powder X-ray diffraction technique, $0.96 < x < 1.04$. No substitution of Sr by Ca or Ba was possible.

The accidental incorporation of Al in the Fe site in the single crystal led to the exploration of Al substitution in compositions $LaSr_3(Fe_{1-x}Al_x)_3O_{10-\delta}$. When $x \leq 0.25$, single-phase material is prepared by reacting the starting oxides at 1400°C. When $x > 0.25$, a second phase begins to appear.

Acknowledgments

The first three authors acknowledge the support of the Robert A. Welch Foundation of Houston, Texas.

Research by S.P. and J.D.J. is supported by the U.S. Department of Energy, Basic Energy Sciences/Materials Sciences under Contract W-31-109-ENG-38. W.M.R. thanks the Northeastern University Research and Scholarship Development and Biomedical Support Funds for support to purchase a cobalt-57 Mössbauer spectroscopy source.

References

1. B. Aurivillius, *Arkiv f. Kemi* **1,** 463 (1949).
2. B. Aurivillius, *Arkiv f. Kemi* **1,** 499 (1949).
3. B. Aurivillius, *Arkiv f. Kemi* **2,** 519 (1950).
4. S. N. Ruddlesden and P. Popper, *Acta Crystallogr.* **11,** 54 (1958).
5. D. Samaras, A. Collomb, and J. Joubert, *J. Solid State Chem.* **7,** 337 (1973).
6. M. N. Deschizeaux Cheruy and J. C. Joubert, *J. Solid State Chem.* **40,** 14 (1981).
7. N. Nguyen, L. Er-Rakho, C. Michel, J. Choisnet, and B. Raveau, *Mater. Res. Bull.* **15,** 891 (1980).
8. L. Er-Rakho, C. Michel, Ph. Lacorre, and B. Raveau, *J. Solid State Chem.* **73,** 531 (1988).
9. J. S. Kim, J. Y. Lee, J. S. Swinnea, H. Steinfink, W. M. Reiff, P. Lightfoot, S. Pei, and J. D. Jorgensen, *J. Solid State Chem.* **90,** 331 (1991).
10. C. Brisi and P. Rolando, *Ann. Chim. (Rome)* **59,** 385 (1969).
11. W. T. Fu, H. W. Zandbergen, Q. Xu, J. M. van Ruitenbeek, L. J. de Jongh, and G. van Tendeloo, *Solid State Commun.* **70,** 1117 (1989).
12. K. Mader and Hk. Muller-Buschbaum, *J. Less-Common Metals* **157,** 71 (1990).
13. M. M. Elcombe, E. H. Kisi, K. D. Hawkins, T. J. White, P. Goodman, and S. Matheson, *Acta Crystallogr. B* **47,** 305 (1991).
14. M. Itoh, M. Shikano, R. Liang, H. Kawaji, and T. Nakamura, *J. Solid State Chem.* **88,** 597 (1990).
15. A. Nozaki, H. Yoshikawa, T. Wada, H. Yamauchi, and S. Tanaka, *Phys. Rev. B* **43,** 181 (1991).
16. W. Gong, J. S. Xue, and J. E. Greedan, *J. Solid State Chem.* **91,** 180 (1991).
17. N. Ohashi, Y. Teramoto, H. Ikawa, O. Fukunaga, and J. Tanaka, *J. Solid State Chem.* **97,** 434 (1992).
18. D. J. Wehe, W. R. Busing, and H. A. Levy, "Program ORABS," ORNL, TM 229, Oak Ridge, TN (1962).
19. S. M. Sheldrick "SHELX 76, Program for Crystal Structure Determination," University of Cambridge, England (1976).
20. "International Tables for X-Ray Crystallography," Vol. IV, Kynock Press, Birmingham (1974). (Present distributor Kluwer, Dordrecht).
21. J. D. Jorgensen, J. Faber, Jr., J. M. Carpenter, R. K. Crawford, J. R. Haumann, R. L. Hitterman, R. Kleb, G. E. Ostrowski, F. J. Rotellà, and T. G. Worlton, *J. Appl. Crystallogr.* **22,** 321 (1989).
22. R. B. Von Dreele, J. D. Jorgensen, and C. G. Windsor, *J. Appl. Crystallogr.* **15,** 581 (1982).
23. J. Y. Lee, J. S. Swinnea, and H. Steinfink, *Acta Crystallogr. C* **47,** 1532 (1991).
24. I. D. Brown and D. Altermatt, *Acta Crystallogr. B* **41,** 244 (1985).
25. V. Russo and G. J. Long, "Mössbauer Spectroscopy Applied to Inorganic Chemistry," Vol. 2, Chap. 6, p. 292, Plenum, New York, 1989.
26. W. M. Reiff, J. Y. Lee, and H. Steinfink, *Z. Anorg. Allgem. Chem.*, **616,** 172 (1992).